Ion-Wind Effects on Poiseuille and Blasius Flow

J. R. Van Rosendale*
University of Utah, Salt Lake City, Utah
M. R. Malik†
High Technology Corporation, Hampton, Virginia
and
M. Y. Hussaini‡
NASA Langley Research Center, Hampton, Virginia

In order to study the effects of ion wind on the plane Poiseuille flow in a channel and Blasius flow on a flat plate, the equations of electrogasdynamics are solved numerically under the assumptions that the flow is incompressible, that the electric field is steady, and that the fluid velocity is negligible compared to ion drift velocity. The results show that ion wind strongly affects the skin-friction distribution for these flows.

I. Introduction

THE phenomenon of corona or ion wind pertains to the bulk motion of a fluid under the influence of an electrostatic force. Over the years, the concept of ion wind has found several engineering applications in heat and mass transfer problems.[1-3] For instance, it has been observed that proper generation of ion wind can augment heat transfer by as much as 200%. Other studies in boundary-layer flows have shown that the ion wind can prevent flow separation and even delay the transition to turbulence. In these studies, the ion wind (generated by external electrodes) is directed towards the wall, and its effect on the wall parameters, such as the heat transfer coefficient, decreases as the freestream velocity increases.

When seeking to use ion wind for the purpose of drag reduction, the corona electrodes may be imbedded in an otherwise insulated surface, and the ground may be either virtual or provided by some remote part of the surface itself. In such a situation the ion wind will provide a "blowing" effect at the wall with no net mass transfer through the wall. Theoretically, the problem is an extremely difficult one in view of the scanty knowledge of the physics of corona discharge near a surface. Before embarking on a study of a rather ambitious use of ion wind for drag reduction in configuration aerodynamics, the complex mechanisms involved in a corona discharge must be well understood. With this purpose in mind, we have carried out a theoretical investigation for simple flow and electrode geometries. The numerical computations are performed within the framework of the two-dimensional incompressible Navier-Stokes and the approximate Maxwell equations for channel and boundary-layer flows.

Corona Discharge

In his book on electrical coronas, Loeb[4] describes corona discharge as "the general class of luminous phenomena appearing associated with the current jump to some microamperes at the highly stressed electrode preceding the ultimate spark breakdown of the gap."

Both dc and ac fields can be used to produce corona discharge if the applied field exceeds a certain threshold. The discharge is characterized as either unipolar or bipolar according to whether one or both electrodes are active. A unipolar corona is called positive or negative according to the polarity of the active electrode. It is instructive to consider a positive point-to-plane corona configuration such as the one depicted in Fig. 1. The positive stressed electrode is surrounded by a thin ionization region where free charges are produced. It is impossible to initiate this charge production without the presence of free trigger electrons. Fortunately, natural ionizing events and cosmic rays create about 20 ion-electron pairs/cm^3/s in air, which is adequate to initiate the process in positive point corona.[4] Other means such as radioactivity, ultraviolet light, and surface treatment could also be used to provide the free charge as needed. The trigger electrons from the interelectrode space are drawn towards the corona electrode, and, there in the high electric field, they generate many electron-positive ion pairs by collisions. This results in an electron avalanche (known as the Townsend avalanche) which is responsible for a sustained corona discharge. The electron avalanches move toward the discharge, leaving behind the positive ions formed during the process. These positive ions drift towards a relatively low electric field denoted as the drift region in Fig. 1 and impart their momentum to the neutral gas molecules by collisions. This results in the motion of the fluid as a whole and is known as the ion or corona wind. Ion wind velocities up to the order of 2 m/s have been reported.[5,6]

The ions do not acquire sufficient energy to produce either significant ionization in the gas or electron ejection at the cathode. The drift region is usually dominated by ions of one sign determined by the polarity of the corona electrode.[7]

II. Governing Equations

We consider the flow of an incompressible fluid under the influence of an electric field. The relevant equations of motion are the usual Navier-Stokes equations with an external body force term which models in the continuum framework the collisions of positive (negative in case of negative corona) ions with the neutral molecules of the fluid. For a homogeneous medium, this force term f is the Coulomb force given by[8]

$$f = -\rho_c^* \nabla \phi^* \tag{1}$$

Received Aug. 15, 1986; revision received July 13, 1987.

*Assistant Professor, Computer Science Department.
†President. Senior Member AIAA.
‡Chief Scientist, Institute for Computer Applications in Science and Engineering. Associate Fellow AIAA.

where ρ_c^* is the dimensional space charge density and ϕ^* the scalar electric potential. This external force term is calculated from the equations for the space charge density and electric potential:

$$\nabla\phi \cdot \nabla\rho_c = \lambda\rho_c^2 \tag{2}$$

$$\nabla^2\phi = -\lambda\rho_c \tag{3}$$

where the electrical potential ϕ and charge density ρ_c have been made nondimensional with reference to their respective values at the corona electrode (denoted by subscript "0"), and λ represents the ratio of electric field produced by space charges to the average electrostatic field and is given by

$$\lambda = \rho_{c_0} L^2/(\phi_0\,\epsilon) \tag{4}$$

ϵ being the electric permittivity of the fluid, ϕ_0 the source voltage, ρ_{c_0} the source charge density, and L a reference length. The above equations are derived from the Maxwell's equations[8,9] under the following assumptions: 1) The effect of the magnetic field caused by the corona current is negligible, 2) Corona discharge is steady (implying constant discharge current), and 3) The fluid velocity is negligible compared to ion drift velocity.

The last of these assumptions is valid at low speeds[10] only. Higher fluid velocities influence the corona current[11] and in that case Eqs. (2) and (3) become coupled with the Navier-Stokes equations. In the present numerical study, however, this interaction is ignored so that the current density j at any point in the field can be represented as

$$j = -\frac{\rho_{c_0}\phi_0 k}{L}\rho_c \nabla\phi \tag{5}$$

where k is the ionic mobility.

Strictly speaking, Eqs. (2) and (3) are valid only in the ion drift region and not in the region immediately surrounding the electrode where the electron avalanche process is active. In this study, we assume that the discharge zone is extremely thin and the above equations are valid all the way to the electrode. Furthermore, two-dimensional electrode geometries are considered in numerical computations. In a cartesian coordinate system (x,y) Eqs. (2) and (3) reduce to

$$\frac{\partial\phi}{\partial x}\frac{\partial\rho_c}{\partial x} + \frac{\partial\phi}{\partial y}\frac{\partial\rho_c}{\partial y} = \lambda\rho_c^2 \tag{6}$$

$$\frac{\partial^2\phi}{\partial x^2} + \frac{\partial^2\phi}{\partial y^2} = -\lambda\rho_c \tag{7}$$

The two-dimensional Navier-Stokes equations are written in the vorticity-streamfunction (ξ,ψ) formulation as

$$\frac{\partial\xi}{\partial t} + u\frac{\partial\xi}{\partial x} + v\frac{\partial\xi}{\partial y} = \frac{1}{R}\left(\frac{\partial^2\xi}{\partial x^2} + \frac{\partial^2\xi}{\partial y^2}\right) + \left(\frac{u_c}{u_e}\right)^2\left(\frac{\partial\rho_c}{\partial x}\frac{\partial\phi}{\partial y} - \frac{\partial\rho_c}{\partial y}\frac{\partial\phi}{\partial x}\right) \tag{8}$$

$$\frac{\partial^2\psi}{\partial x^2} + \frac{\partial^2\psi}{\partial y^2} = \xi \tag{9}$$

$$(u,v) = \left(\frac{\partial\psi}{\partial y}, -\frac{\partial\psi}{\partial x}\right) \tag{10}$$

Here $u_c = \sqrt{\phi_0\,\rho_{c_0}/\rho}$ is a characteristic velocity and R is the Reynolds number defined as

$$R = \rho u_e L/\mu \tag{11}$$

where u_e is the reference velocity, ρ the fluid density, and μ the viscosity.

Equations (6–10) are the governing equations for the electrogasdynamics (EGD) of the ion wind in two dimensions. The boundary conditions depend upon the gemoetry of the particular problem.

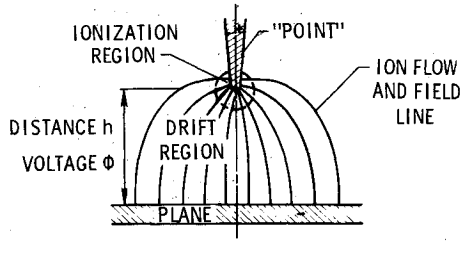

Fig. 1 Schematic of a positive point-to-plane corona gap.

III. The Solution Procedure

The fundamental difficulty in solving the electrostatic problem is that the parameter λ appearing in Eqs. (6) and (7) is not known a priori. Given a configuration and a source of voltage ϕ_0, this essentially means that the source charge density ρ_{c_0}, which is needed to solve the hyperbolic equation for space charge density, i.e., Eq. (2), is unknown. This arbitrariness in the problem comes about because the complex interactions in the active corona region (ionization region in Fig. 1 which is bipolar as described in the introduction) are not modeled and the unipolar govering equations [Eqs. (2–3)] are assumed valid all the way to the electrode. This makes it necessary to provide information in addition to the boundary conditions for the electric potential. Following Ref. 12, we assume that the total discharge current is known, say, from a laboratory experiment. We iterate on λ until the total current reaching the cathode, calculated form Eqs. (5–7), balances the known discharge current. This essentially implies that for a

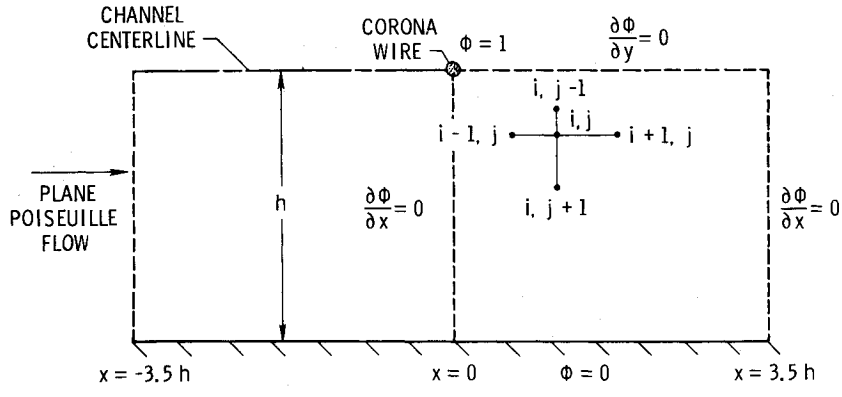

Fig. 2 Computational domain for the EDG channel problem.

given ϕ_0 there is a unique value of the source charge density ρ_{c_0} that will give a current distribution on the cathode whose integral is equal to the known discharge current. If the problem of bipolar conduction is considered, there will be no need for the prior knowledge of the discharge current. This is, however, outside the scope of the present study.

We shall consider the problem in which the corona electrode is a thin wire of infinite length, and the cathode is a flat plate. The corona wire is placed laterally either on the centerline of a channel (see Fig. 2) or is imbedded in an insulated surface (see Sec. IV for Blasius boundary layer).

In Fig. 2, the computation domain for the channel problem is shown. The flow is from left to right. In the cartesian coordinate system chosen for the study, x is along the channel while y is across it. The channel height is $2h$. In the present case, $y = 0$ represents one of the channel walls (which serve as cathodes) and $y = h$ is the centerline. The corona wire (or the anode) is located at $x = 0$, $y = h$. The boundary conditions for this problem are

$$\frac{\partial \phi}{\partial x} = 0 \tag{12a}$$

at a plane of symmetry or far away from the corona wire

$$\frac{\partial \phi}{\partial y} = 0 \tag{12b}$$

at a plane of symmetry or the flat plate for Blasius boundary layer

$$\phi = 0 \tag{12c}$$

at the cathode

$$\phi = 1 \tag{12d}$$

at the anode (corona wire).

The usual five-point difference operator is used to discretize the electric potential Eq. (7) for uniform grid. For stretched grids, we use a variant of this method to ensure second-order accuracy. The solution to the discretized equation is obtained by successive over relaxation (SOR).

As suggested in Ref. 12, the space charge density Eq. (6) is discretized using backward differences for ρ_c and central differences for ϕ. The solution for ρ_c is then obtained by marching from the anode to the cathode and is given as (see Fig. 2 for an explanation of the subscripts i, j)

$$\rho_{c_{i,j}} = b + \sqrt{b^2 - c} \tag{13}$$

where

$$b = \frac{1}{2\lambda}\left[\frac{1}{\Delta x}\frac{\partial \phi}{\partial x}\bigg|_{i,j} + \frac{1}{\Delta y}\frac{\partial \phi}{\partial y}\bigg|_{i,j}\right]$$

and

$$c = \frac{1}{\lambda}\left[\frac{1}{\Delta x}\frac{\partial \phi}{\partial x}\bigg|_{i,j}\rho_{c_{i-1,j}} + \frac{1}{\Delta y}\frac{\partial \phi}{\partial y}\bigg|_{i,j}\rho_{c_{i,j-1}}\right]$$

Note that the Neumann boundary conditions on the electric potential [Eq. (12)] at a plane of symmetry facilitate the computation of ρ_c (in Fig. 2) along the plane $x = 0$, $0 \le y < h$ and $0 < x \le 3.5h$, $y = h$. These values of ρ_c are needed in the expression for c above to march the solution away from the anode.

Fluid Problem

In the vorticity transport Eq. (8), the time advancement is done by the Dufort-Frankel method,[13] and the advection-diffusion terms are discretized by a weighted mean scheme.[14] For instance, the finite difference approximation of the spatial derivatives in the x-direction is as follows:

$$\left(\frac{1}{R}\frac{\partial^2 \xi}{\partial x^2} - u\frac{\partial \xi}{\partial x}\right) = \alpha_{i+1}\,\xi_{i+1} + \alpha_{i-1}\xi_{i-1} - (\alpha_{i+1} + \alpha_{i-1})\xi_i \tag{14}$$

where

$$\alpha_{i+1} = \frac{u_{i+\frac{1}{2}}}{x_{i+1} - x_{i-1}}\left[\coth(\theta_{i+\frac{1}{2}}) - 1\right]$$

$$\alpha_{i-1} = \frac{u_{i-\frac{1}{2}}}{x_{i+1} - x_{i-1}}\left[\coth(\theta_{i-\frac{1}{2}}) + 1\right]$$

with

$$\theta_{i+\frac{1}{2}} = u_{i+\frac{1}{2}}(x_{i+1} - x_i)R$$

and

$$\theta_{i-\frac{1}{2}} = u_{i-\frac{1}{2}}(x_i - x_{i-1})R$$

In the case of a one-dimensional steady advection-diffusion equation with constant coefficients, the numerical solution of the discretized equation agrees identically at the nodes with the exact solution, showing that boundary layers will be effectively resolved. The boundary conditions for vorticity are

$$\xi = \xi(y) \tag{15a}$$

at inflow

$$\frac{\partial^2 \xi}{\partial x^2} = 0 \tag{15b}$$

at outflow

$$\xi = \frac{\partial^2 \psi}{\partial y^2} \tag{15c}$$

at the wall

$$\xi = 0 \tag{15d}$$

at channel centerline or the freestream.

Both the outflow and the wall boundary conditions are imposed by second-order accurate finite-difference formulas.

The boundary conditions for the streamfunction are

$$\psi = \psi(y) \tag{16a}$$

at inflow

$$\frac{\partial^2 \psi}{\partial x^2} = 0 \tag{16b}$$

at outflow

$$\psi = 0 \tag{16c}$$

at the wall

$$\psi = 1 \tag{16d}$$

at channel centerline or

$$\frac{\partial \psi}{\partial y} = 1 \tag{16e}$$

in the freestream.

The streamfunction Eq. (9) is discretized by the usual five-point difference formula for the uniform grid. In order to retain second-order accuracy on the highly stretched grids needed for boundary layer resolution, a variant of the five-point formula derived from piecewise linear finite-element methods is used. This representation is second-order accurate even if the mesh spacing changes abruptly. The discretization based on piecewise linear finite elements is obtained on the triangular grid formed by adding a diagonal

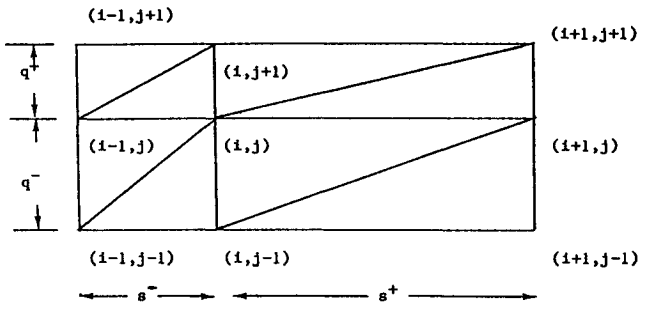

Fig. 3 Triangular grid for piecewise linear finite elements.

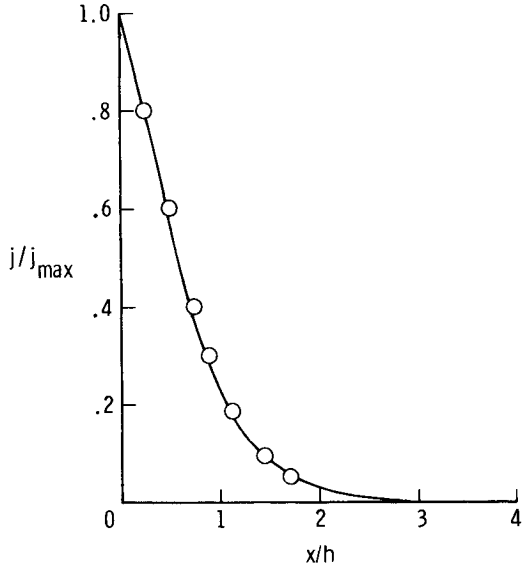

Fig. 4 Comparison of computed (solid line) peak normalized current density distribution on the cathode plate with the experimental data of Yamamoto[17] (open symbols), $\phi_0 = 15$ kv.

Table 1 Effect of the grid size on the average skin friction with one corona wire, $\phi_0 = 15$ kv

Grid Size	$C_{f_{av}}$
65 × 17	0.001464
65 × 33	0.001406
129 × 33	0.001363
257 × 65	0.001362

to each rectangular cell, as shown in Fig. 3. The resulting formula requires initial scaling of the vorticity ξ according to

$$s = (1/2)(s^+ + s^-),\ q = (1/2)(q^+ + q^-)$$

$$\tilde{\xi}_{ij} = (1/2)sq\,\xi_{ij} + (1/12)s^+q^+\,\xi_{i+1,j+1} + (1/12) \times s^-q^-\xi_{i-1,j-1} + (1/12)s^+\,q\xi_{i+1,j} + (1/12)s^-\,q\,\xi_{i-1,j} + (1/12)\,sq^+\,\xi_{i,j+1} + (1/12)\,sq^-\,\xi_{i,j-1} \tag{17}$$

Then the discretization of the Poisson equation becomes as follows:

$$\frac{q}{s^+}\psi_{i+1,j} + \frac{q}{s^-}\psi_{i-1,j} + \frac{s}{q^+}\psi_{i,j+1} + \frac{s}{q^-}\psi_{i,j-1} - 8\frac{sq}{s^+s^- + q^+q^-}\psi_{i,j} = \tilde{\xi}_{i,j} \tag{18}$$

The asymmetry in the scaling of ξ above comes from the orientation of the diagonal in the rectangles. Averaging over the two possible orientations, we set the alternate scaling:

$$\tilde{\xi}_{i,j} = (1/2)\,sq\xi_{i,j} + (1/24)\,s^+\,q^+\,\xi_{i+1,j+1} + (1/24)\,s^+\,q^-\,\xi_{i+1,j-1} + (1/24)\,s^-\,q^+\,\xi_{i-1,j+1} + (1/24)\,s^-\,q^-\,\xi_{i-1,j-1} + (1/12)\,s^+\,q\,\xi_{i+1,j} + (1/12)\,s^-\,q\,\xi_{i-1,j} + (1/12)\,sq^+\,\xi_{i,j+1} + (1/12)\,sq^-\,\xi_{i,j-1} \tag{19}$$

The resulting Poisson discretization is second-order on any tensor product grid and is found to work well in practice. Since the difference star operating on the solution function ψ here is just the five-point star, performing iterations with these formulas is almost as inexpensive as the usual finite difference formulas, though the formulas are more accurate.

The linear systems resulting from this discretization were solved by a multigrid code based on zebra-line relaxation.[15] It is well known that point iterative algorithms, such as the SOR iteration, perform poorly on highly stretched grids like those employed here. Alternating direction iterations, such as the zebra iteration used here, provide rapid smoothing even on stretched grids.[15] There are four steps in a complete zebra relaxation. One must perform line SOR iteration on even-numbered x-lines, even y-lines, odd x-lines, and odd y-lines. This ordering of steps is used in the zebra iteration here, although little difference was observed when the ordering was altered. We also experimented with other splittings, such as the ADI factorization. In this multigrid context, these alternative splittings seem to offer no advantage.

The use of zebra smoothing iteration, coupled with the projection and injection operations arising naturally in the finite element context lead to a fast and robust algorithm.[16] When a Poisson solver is used in time-dependent problems, a good starting value is always available from the previous time step. In this situation, a multigrid algorithm performing two full zebra sweeps on each multigrid level at each time step seems more than adequate. Fast convergence of the Poisson equation was observed on all tensor product grids tried, as long as the mesh spacing changed slowly from one mesh cell to the next. That is, the cell aspect ratios s/q could be arbitrarily large without hampering convergence, as long as s and q varied slowly from cell to cell.

IV. Computational Results

Plane Poiseuille Flow

Figure 2 provides a sketch of the flow and electrode configuration. The main reason for the choice of this problem is the availability of experimental results for the electric field.[17] For drag reduction in confined flows, discrete discharging electrodes should not be on the surface (surface blowing in confined flows increases skin friction) but rather along the centerline to provide a "wall suction" effect. The mathematical problem considered is that of the incompressible flow of air between two parallel plates (serving as cathodes) with one lateral wire anode kept at a potential $\phi_0 = 15$ kv with respect to the plates. The wire-to-plate distance h is 3 cm. The electrical permittivity ϵ is 8.85×10^{-12} A-s/v-m whereas the mobility coefficient k for positive ions in air is taken as 0.00014 m^2/v-s. The total discharge current for this case was taken from Ref. 17 to be 210 μA/m. Figure 4 shows the peak normalized current density distribution on the cathode plate (i.e., the channel wall). Although the peak is not properly resolved in the computations, the current density distribution is in general agreement with the experimental data of Yamamoto.[17] In Fig. 5, the electrical potential distributions in the region between the wire and the plate are presented for $x/h = 0$, 0.4, and 0.8. The agreement between the computa-

tion and the experimental data of Yamamoto[17] is good for $y/h \gtrsim 0.4$. Relatively poor agreement for smaller values of y/h may be attributed to the approximations admitted in the electrostatic problem which involve ignoring bipolar conduction in the active corona region.

The calculated vorticity and streamfunction distributions are presented in Fig. 6, showing the qualitative nature of the flow streamlines and constant vorticity contours for a Reynolds number of 3600. The computational box extended from $x = -3.5h$ to $x = 3.5h$ with the corona wire located midway across the centerline (i.e., at $x = 0$, $y = h$). There is a small reverse flow region near the wall around $x = 0$. The curl of the Coulomb force [see Eq. (1)] is nonzero, and therefore vorticity is generated. The strong vorticity concentration observed in Fig. 6 is due to the fact that ion wind has a larger effect near the wall since the velocities due to plane Poiseuille flow alone are small there—an obvious result of no-slip boundary conditions. In the absence of plane Poiseuille flow ($R = 0$), ion wind alone generates two counter-rotating cells (in x-y plane) between the channel wall (cathode) and the channel centerline. For $R \neq 0$, the cell generated ahead of the corona wire results in flow reversal near the wall while generating an accelerated flow away from it. The size of the reverse flow region decreases as R increases.

The time step for the vorticity equation was calculated by $\Delta t = 0.9\ \Delta x/u_{\max}$. In this case with 129×33 uniformly spaced points, the steady state solution was achieved in about 800 steps. The criteria for convergence in all the calculations was that

$$\max\left|\frac{\partial \xi}{\partial t}\right| < \min(\Delta x^2,\ \Delta y^2)$$

Figure 7 displays the calculated skin-friction distribution with one corona wire along with that for the fully developed channel value ($C_f = 6/R$). In the region ahead of the wire, the flow is directed towards the wire and away from the wall resulting in lower skin friction. The situation is reversed in the region after the wire; the distribution is not symmetric, however, due to flow bias. Here the skin friction was calculated directly from the wall vorticity.

For a Reynolds number $R = 3600$, calculations were made using 65×17, 65×33, 129×33, and 257×65 points. In order to calculate the average drag coefficient, the skin friction was integrated over the length of the computational box ($= 7h$). These results are presented in Table 1. It is clear that sufficiently accurate results are obtained with 129×33 points. Using this same grid, calculations were also made for $R = 5000$ and 6785. The results are presented in Fig. 8 for these Reynolds numbers as percentage change in drag due to the corona discharge:

$$\Delta \text{ DRAG } \% = 100(C_{f_{av}} \times R/6 - 1)$$

As mentioned previously, the average C_f was calculated by integrating over the length of the computational box, and the electrical potential in these calculations is 15 kv. The skin-friction drag has decreased considerably (18.2% at $R = 3600$) over the length of the computational box. The calculated skin friction at the outflow in these computations was about 14% greater than that of the plane Poiseuille value.

The effect of the positioning of the inflow and outflow boundaries was also investigated. With the corona wire

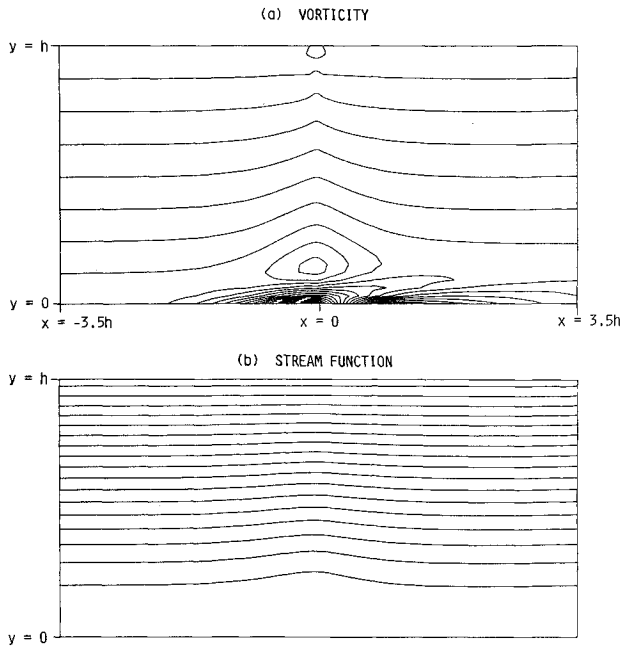

Fig. 6 Calculated vorticity and streamfunction in a channel with one corona wire located across the centerline ($x = 0$, $y = h$). Contour levels for vorticity are from -0.8 to 2.4 in intervals of 0.2, while for streamfunction, levels are from 0.03 to 0.51 in intervals of 0.03.

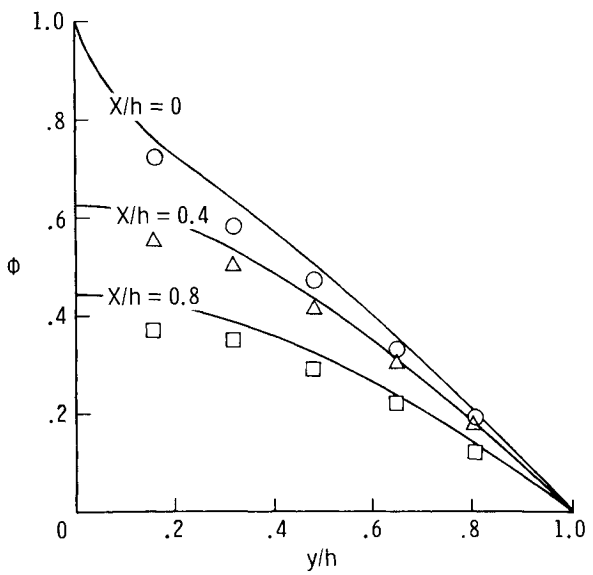

Fig. 5 Comparison of computed (solid line) electrical potential with the experimental data of Yamamoto[17] (open symbols), $\phi_0 = 15$ kv.

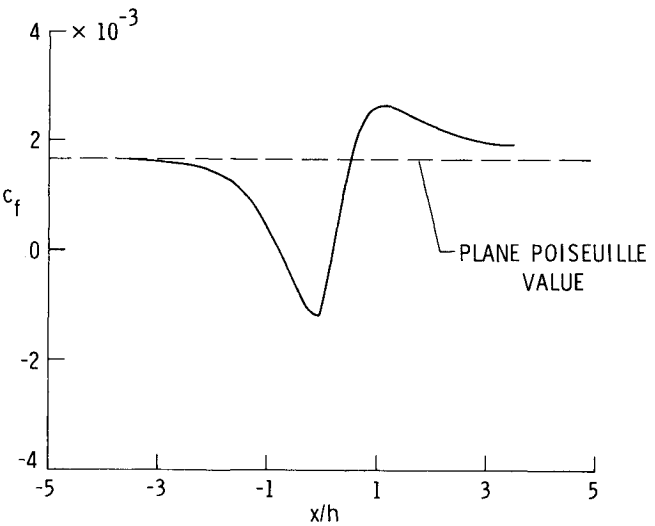

Fig. 7 Wall ($y = 0$) skin friction distribution with one corona wire for the same flow as in Fig. 6; $R = 3600$, $\phi_0 = 15$ kv.

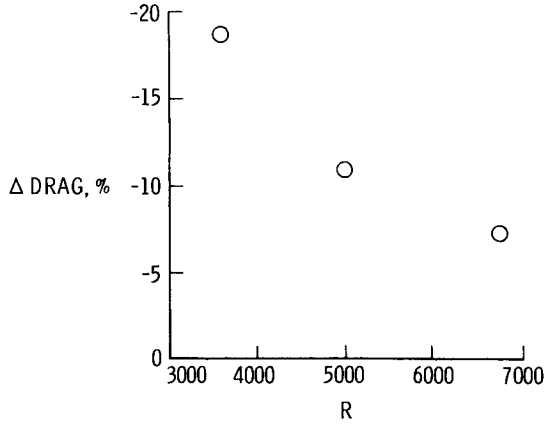

Fig. 8 Percentage reduction in skin friction drag within the computational domain depicted in Fig. 2, $\phi_0 = 15$ kv.

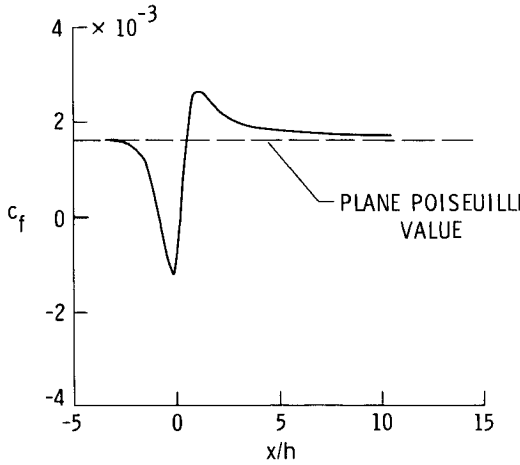

Fig. 9 Skin friction distribution with one corona wire for the extended computational box.

located at $x = 0$ and the electrostatic force present in the region $-3.5h < x < 3.5h$, the inflow and outflow boundaries were placed at $x = -7h$ and $7h$, respectively. For all practical purposes, the solution in the region $-3.5h < x \leq 3.5h$ remained unaffected. The plane Poiseuille flow was recovered in the region $-7h < x \leq -3.5h$. The skin friction relaxed slowly to the channel value in the region $x > 3.5h$. These computations were made with a grid of 257×33 points to retain the same accuracy. In another set of calculations, the computational box extended from $-3.5h$ to $10.5h$, and the corona wire location was unchanged. Again, the solution in the region $-3.5h < x \leq 3.5h$ was unaffected. In the region $x > 3.5h$, the skin friction relaxes slowly to the value for the Poiseuille flow as is evident in Fig. 9. The integrated skin friction indicates that now in the computational region the drag reduction has dropped from 18.2% to only 5%. The skin friction at the outflow is still about 2.8% higher than the Poiseuille value and, if integration continues, the drag reduction will perhaps disappear. The region of reduced drag could be extended, however, by a properly arranged multiwire system.

We have extended the calculation to a two-wire system. In this simulation, the inflow and outflow boundaries were located at $x = -4.3h$ and $x = 4.3h$, respectively. The two wires were placed at $x = \pm 0.8h$, $y = h$ and were at a potential of 15 kv with respect to the channel walls. The discharge current taken from Ref. 17 was 350 μA/m. The calculated vorticity and streamfunction contours are presented in Fig. 10.

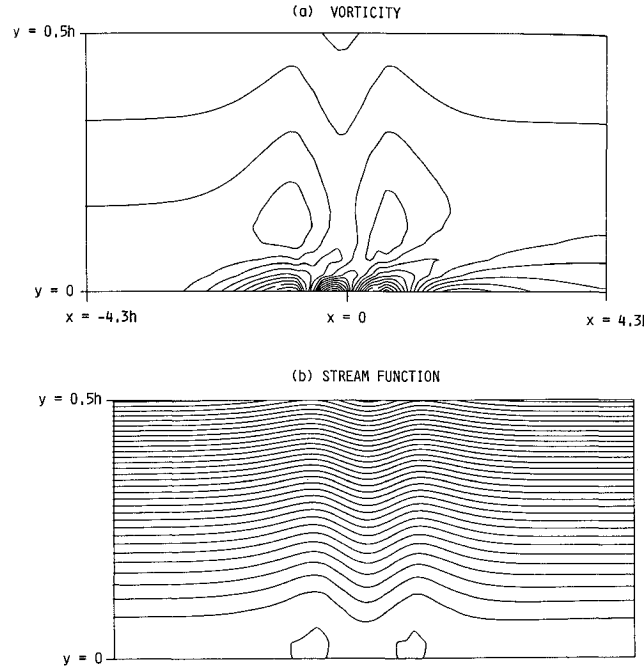

Fig. 10 Calculated vorticity and streamfunction in a channel with two corona wires located at $x = \pm 0.8h$. Contour levels for vorticity are from -1.5 to 6.5 intervals of 0.5; while for streamfunction, levels are from 0 to 0.31 in intervals of 0.01.

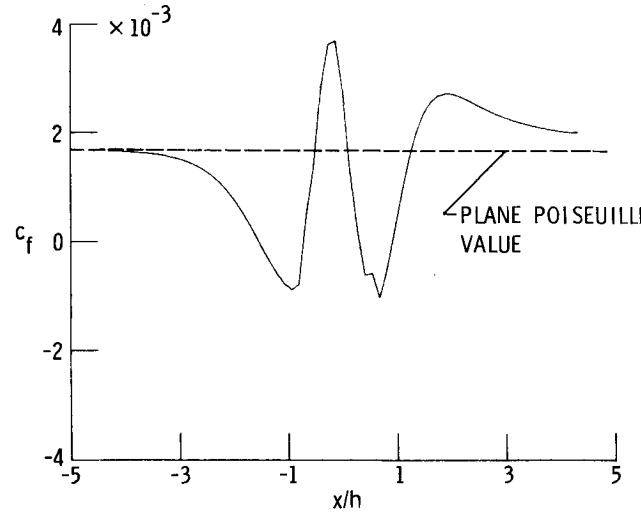

Fig. 11 Skin friction distribution with two corona wires.

Only the region $0 < y < 0.5h$ is shown to give a clearer picture of the near-wall flow. Note the wavy pattern of streamfunction near the wall due to repeated deceleration and acceleration of the flow in the presence of corona wires. As a consequence, the skin-friction distribution also has a wavy behavior (see Fig. 11). The integration of these results, obtained with a 65×33 grid, indicates a drag reduction of 15.5%. The corresponding reduction for one-wire system was also about the same. Results presented in Table 1 suggest that the decrease in drag will be slightly higher with a refined mesh.

Blasius Boundary Layer

We now consider a Blasius boundary layer with the corona wire embedded laterally in the flat. The cathode is assumed to be an imaginary surface (i.e., the flow does not see it) at a

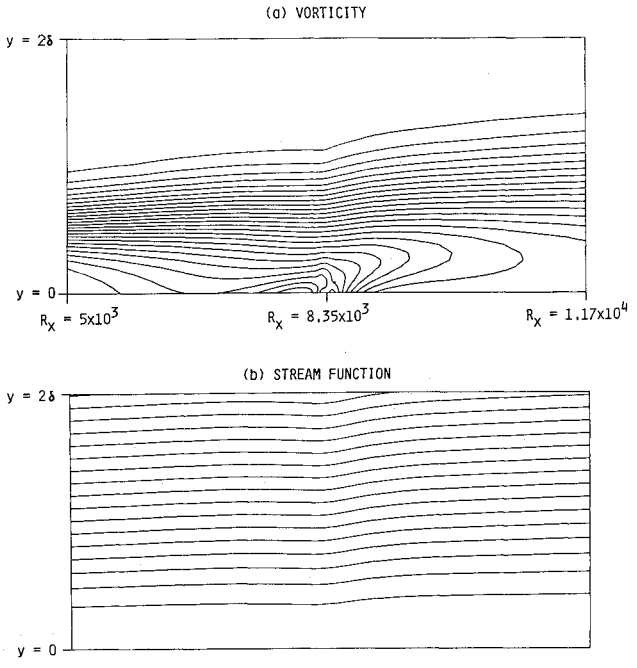

Fig. 12 Calculated vorticity and streamfunction in a boundary layer with one corona wire imbedded in the insulated wall at $y = 0$, $R_x = 8.35 \times 10^3$. Contour levels for vorticity are from 1 to 25 in intervals of 1; while for streamfunction, levels are from 0.007 to 0.119 in intervals of 0.007.

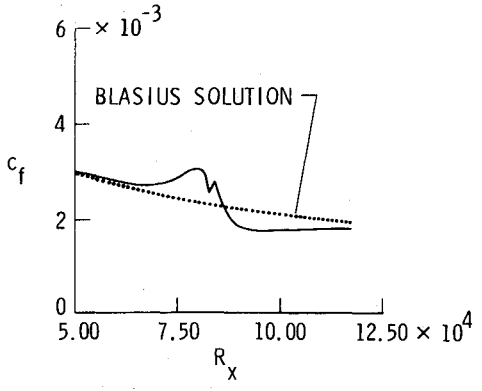

Fig. 13 Skin friction distribution for a boundary layer with one corona wire, $\phi_0 = 15$ kv.

certain distance from the plate, and we assume that surface to be flat. Due to lack of knowledge of physics of corona near an insulated surface, it seems reasonable to assume that the model used in the case of the channel flow holds for this configuration also.

The magnitude of the corona current is chosen arbitrarily as the experimental value is not available. However, for a given electric potential and interelectrode spacing, the solution of the EGD equations seems to converge only for a particular range of currents.

The top boundary in these computations was placed at about 10δ, δ being the boundary layer thickness, and computations were made on a 101×51 grid. A highly stretched grid was used to resolve the boundary layer properly. Figure 12 gives the calculated vorticity and streamfunction distribution. The inflow in this case was prescribed by solving the Blasius equation by a second-order accurate two-point compact difference scheme. The wire potential was assumed to be 15 kv and the current was 100 μA/m. The skin-friction distribution is presented in Fig. 13. There is local departure from the Blasius solution; however, no overall change in drag is noticed. The effect of ion wind on the skin friction is opposite to that in the plane Poiseuille case since the corona wire is now on the surface. The skin friction now increases ahead of the wire and decreases after it. Several other electric potential/current combinations were tried with similar results. Since these results for the boundary layer are obtained with a rather crude model of the electrical problem, it is worthwhile to examine the situation experimentally to gain insight into the physics of corona discharge near a surface and develop models for corona discharge based, perhaps, on electron avalanches.[18] Some experimental results were reported in Ref. 19.

V. Concluding Remarks

We have presented theoretical results relating the effect of ion wind on viscous drag. We have found that skin-friction distribution is strongly affected by the presence of ion wind. Our results indicate drag reductions of the order of 20% (within the computational domain) for an applied voltage of 15 kv in plane Poiseuille flow at low speeds. The laminar boundary-layer calculations did not show any such reductions. This may be ascribed, however, to the particular model of the corona discharge that we used for the boundary layer. The required experimental input for proper simulation of the corona discharge in the boundary layer is not available. More systematic experimental and theoretical investigations should be carried out before a definitive statement regarding drag reduction can be made.

Acknowledgment

Research was sponsored by the National Aeronautics and Space Administration in part under NASA Contract NAS1-15810 for the first author; NASA Contracts NAS1-16916 and NAS1-18240 for the second author; and NASA Contracts NAS1-15810, NAS1-16394, NAS1-17070, and NAS1-18107 for the third author.

References

[1]Velkoff, H. R., "Evaluating the Interactions of Electrostatic Fields with Fluid Flows," American Society of Mechanical Engineers, New York, Paper 71-DE-41, 1971.

[2]Velkoff, H. R. and Kulacki, F. A., "Electrostatic Cooling," American Society of Mechanical Engineers, New York, Paper 77-DE-36, 1977.

[3]Kibler, K. G. and Carter, H. G., Jr., "Electro-cooling in Gases," *Journal of Applied Physics*, Vol. 45, 1974, pp. 4436-4440.

[4]Loeb, L. B., *Electrical Coronas*, University of California Press, Berkeley, CA, 1965.

[5]Sato, T., "Drift Velocity Measurements of Charged Particles Under Corona Discharge in Air Gap I," *Journal of Electrostatics*, Vol. 8, 1980, pp. 271-278.

[6]Ramadan, O. E. and Soo, S. L., "Electrohydrodynamic Secondary Flow," *The Physics of Fluids*, Vol. 12, 1969, pp. 1943-1945.

[7]Goldman, M. and Sigmond, R. S., "Corona and Insulation," *IEEE Transactions on Electrical Insulation*, Vol. EI-17, No. 2, April 1982.

[8]Woodson, H. H. and Melcher, J. R., *Electromechanical Dynamics*, Wiley Inc., New York, NY, 1968.

[9]Stuetzer, O. M., "Magnetohydrodynamics and Electrohydrodynamics," *The Physics of Fluids*, Vol. 5, 1962, pp. 534-544.

[10]Yamamoto, T. and Velkoff, H. R., "Electrohydrodynamics in an Electrostatic Precipitator," *Journal of Fluid Mechanics*, Vol. 108, 1981, pp. 1-18.

[11]Chapman, S., "The Magnitude of Corona Point Discharge Current," *Journal of the Atmospheric Sciences*, Vol. 34, 1977, pp. 1801-1809.

[12]Leutert, G. and Bohlen, B., "The Spatial Trend of Electric Field Strength and Space Charge Density in Plate-Type Electrostatic Precipitators," *Stuab-Reinhalt Luft*, Vol. 32, 1972, pp. 27-33.

[13]Dufort, E. C. and Frankel, S. P., "Stability Conditions in the Numerical Treatment of Parabolic Differential Equations," *Mathematical Tables Aids Computation*, Vol. 7, 1953, pp. 135-152.

[14]Fiadeiro, M. E., and Veronis, G., "On Weighted-Mean Schemes for the Finite-Difference Approximation to the Advection-Diffusion Equation," *Tellus*, Vol. 29, 1977, pp. 512-522.

[15]Brandt, A., "Multilevel Adaptive Solution to Boundary Value Problems," *Mathematics of Computations*, Vol. 31, 1977, pp. 333-391.

[16]Nicolaides, R. A., "On the L^2-Convergence of an Algorithm for Solving Finite Element Equations," *Mathematics of Computation*, Vol. 31, 1977, pp. 892-906.

[17]Yamamoto, T., *Electrohydordynamic Secondary Flow Interaction in an Electrostatic Precipitator*, Ph.D. Dissertation, Ohio State University, Columbus, OH, 1979.

[18]Ibrahim, A. A. and Singer, H., "Calculation of Corona Discharge in Positive Point to Plane Gaps," *Proceedings of the 7th International Conference on Gas Discharges and Their Applications*, Peter Peregrinus, England, 1982, pp. 128-131.

[19]Malik, M. R., Weinstein, L. M., and Hussaini, M. Y., "Ion Wind Drag Reduction," AIAA Paper 83-0231, 1983.